Experimental and *Ab Initio* Ultrafast Carrier Dynamics in Plasmonic Nanoparticles

Ana M. Brown,[1] Ravishankar Sundararaman,[2,3,*] Prineha Narang,[1,2,4,†] Adam M. Schwartzberg,[5] William A. Goddard III,[2,6] and Harry A. Atwater[1,2]

[1]*Thomas J. Watson Laboratories of Applied Physics, California Institute of Technology, 1200 East California Boulevard, Pasadena, California 91125, USA*

[2]*Joint Center for Artificial Photosynthesis, California Institute of Technology, 1200 East California Boulevard, Pasadena, California 91125, USA*

[3]*Department of Materials Science and Engineering, Rensselaer Polytechnic Institute, 110 8th Street, Troy, New York 12180, USA*

[4]*NG NEXT, 1 Space Park Drive, Redondo Beach, California 90278, USA*

[5]*The Molecular Foundry, Lawrence Berkeley National Laboratory, 1 Cyclotron Road, Berkeley, California 94720, USA*

[6]*Materials and Process Simulation Center, California Institute of Technology, 1200 East California Boulevard, Pasadena, California 91125, USA*

(Received 11 August 2016; published 21 February 2017)

Ultrafast pump-probe measurements of plasmonic nanostructures probe the nonequilibrium behavior of excited carriers, which involves several competing effects obscured in typical empirical analyses. Here we present pump-probe measurements of plasmonic nanoparticles along with a complete theoretical description based on first-principles calculations of carrier dynamics and optical response, free of any fitting parameters. We account for detailed electronic-structure effects in the density of states, excited carrier distributions, electron-phonon coupling, and dielectric functions that allow us to avoid effective electron temperature approximations. Using this calculation method, we obtain excellent quantitative agreement with spectral and temporal features in transient-absorption measurements. In both our experiments and calculations, we identify the two major contributions of the initial response with distinct signatures: short-lived highly nonthermal excited carriers and longer-lived thermalizing carriers.

DOI: 10.1103/PhysRevLett.118.087401

Plasmonic hot carriers provide tremendous opportunities for combining efficient light capture with energy conversion [1–5] and catalysis [6,7] at the nanoscale [8–10]. The microscopic mechanisms in plasmon decays across various energy, length, and time scales are still a subject of considerable debate, as seen in recent experimental [11,12] and theoretical literature [13–16]. The decay of surface plasmons generates hot carriers through several mechanisms, including direct interband transitions, phonon-assisted intraband transitions, and geometry-assisted intraband transitions, as we have shown in previous work [17,18].

Dynamics of hot carriers are typically studied via ultrafast pump-probe measurements of plasmonic nanostructures using a high-intensity laser pulse to excite a large number of electrons and measure the optical response as a function of time using a delayed probe pulse [11,19–25]. Various studies have taken advantage of this technique to investigate electron-electron scattering, electron-phonon coupling, and electronic transport [20,22,26–32]. Figure 1 shows a representative map of the differential extinction cross section as a function of pump-probe delay time and probe wavelength. With an increase in electron temperature, the real part of the dielectric function near the resonant frequency becomes more negative, while the imaginary part increases [33]. This causes the resonance to broaden and blueshift at short times as the electron temperature rises rapidly, and then to narrow and shift back over longer times as electrons cool down, consistent with previous observations [34]. Taking a slice of the map at one probe wavelength reveals the temporal behavior of the electron relaxation [Fig. 1(b)], whereas a slice of the map at one time gives the spectral response, as shown in Fig. 1(a) for a set of times relative to the delay time with maximum signal, $t_{\max} = 700$ fs.

Conventional analyses of pump-probe measurements invoke a "two-temperature model" that tracks the time dependence (optionally the spatial variation) of separate electron and lattice temperatures, T_e and T_l, respectively, which implicitly neglects nonequilibrium effects of the electrons. Recent literature has focused on the contributions of thermalized and nonthermalized electrons to the optical signal in pump-probe measurements using free-electron-like theoretical models to interpret optical signatures [20,26,35–38]. However, these models invariably require empirical parameters for both the dynamics and response of the electrons, making unambiguous interpretation of experiments challenging. This Letter quantitatively identifies nonequilibrium ultrafast dynamics of electrons, combining experimental measurements and parameter-free *ab initio* predictions of the excitation and relaxation dynamics of hot carriers in plasmonic metals across time scales ranging from 10 fs to 10 ps. Note that, while metal thin films or single crystals would provide a "cleaner" experimental system in general, we focus on nanoparticles here because they enable an important simplification: electron distributions are constant in space over the length

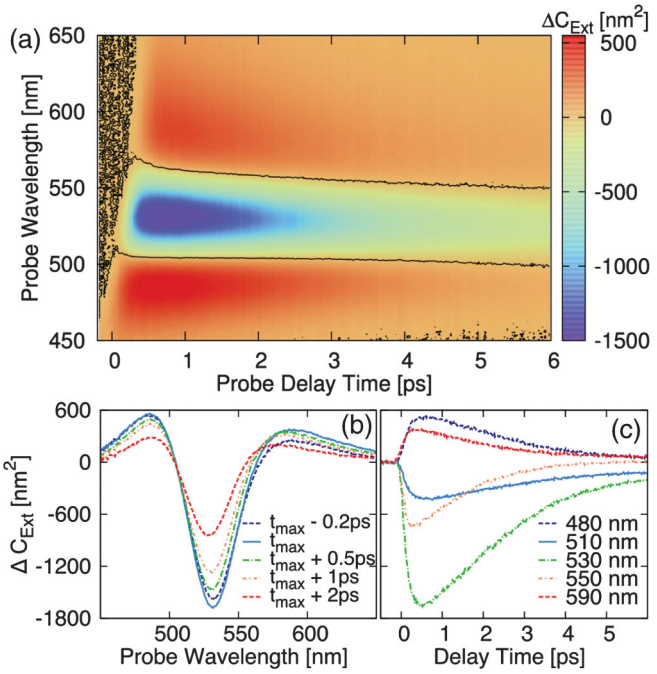

FIG. 1. (a) Map of the differential extinction cross section of colloidal gold nanoparticles as a function of pump-probe delay time and probe wavelength for a pump pulse of 68 μJ/cm^2 energy density at 380 nm. At time 0, the pump pulse excites the sample. As the electrons thermalize internally, extinction near the absorption peak (533 nm) decreases (negative signal) while extinction in the wings to either side of the absorption peak increases (positive signal). After ~700 fs, the electrons began to thermalize with the lattice and the differential extinction decays. A contour line is drawn in black at zero extinction change. Differential extinction (b) as a function of probe wavelength at a set of times relative to the pump-probe delay time with maximum signal, $t_{max} = 700$ fs and (c) as a function of pump-probe delay time at various probe wavelengths.

scale of these particles, allowing us to treat temporal dynamics and optical response in greater detail (see Supplemental Material [39]).

A theoretical description of pump-probe measurements of hot carrier dynamics in plasmonic systems involves two major ingredients: (i) The optical response of the metal (and its environment) determines the excitation of carriers by the pump as well as the subsequent signal measured by the probe pulse; (ii) the dynamics of the excited carriers, including electron-electron and electron-phonon scattering, determines the time dependence of the probe signal. We previously presented [33] *ab initio* theory and predictions for both the optical response and the dynamics within a two-temperature model, where the electrons are assumed to be in internal equilibrium albeit at a different temperature from the lattice. Below, we treat the response and relaxation of nonthermal electron distributions from first-principles calculations, without assuming an effective electron temperature at any stage.

For the optical response, we calculate the imaginary part of the dielectric function Im$\epsilon(\omega)$ accounting for direct interband transitions, phonon-assisted intraband transitions, and the Drude (resistive) response, and calculate the real part using the Kramers-Kronig relations. Specifically, we start with density-functional theory calculations of electron and phonon states as well as electron-photon and electron-phonon matrix elements using the JDFTX code [40], convert them to an *ab initio* tight-binding model using Wannier functions [41], and use the Fermi golden rule and linearized Boltzmann equation for the transitions and Drude contributions, respectively. The theory and computational details for calculating $\epsilon(\omega)$ are presented in detail in Refs. [17,33], and we do not repeat them here. All these expressions are directly in terms of the electron occupation function $f(\varepsilon)$, and we can straightforwardly incorporate an arbitrary nonthermal electron distribution instead of Fermi functions. These nonthermal distributions differ from the thermal Fermi distributions by sharp distributions of photoexcited electrons and holes that dissipate with time due to scattering, as shown in Fig. 2 and discussed below.

We use the *ab initio* metal dielectric function for calculating the initial carrier distribution as well as the probed response. The initial carrier distribution following the pump pulse is given by

$$f(\varepsilon, t=0) = f_0(\varepsilon) + U\frac{P(\varepsilon,\hbar\omega)}{g(\varepsilon)}, \qquad (1)$$

where f_0 is the Fermi distribution at ambient temperature, U is the pump pulse energy absorbed per unit volume, $g(\varepsilon)$ is the electronic density of states [33], and $P(\varepsilon,\hbar\omega)$ is the energy distribution of carriers excited by a photon of energy $\hbar\omega$ [17]. We then evolve the carrier distributions and lattice temperature in time to calculate $f(\varepsilon,t)$ and $T_l(t)$ as

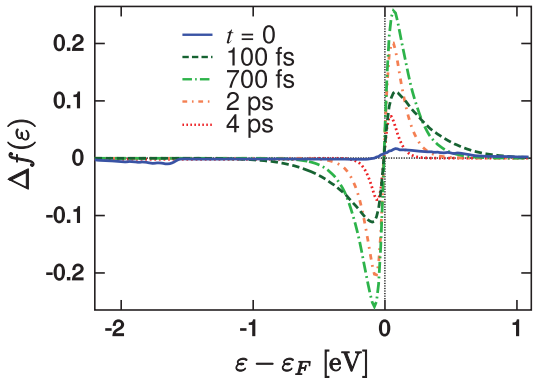

FIG. 2. Difference of the predicted time-dependent electron distribution from the Fermi distribution at 300 K, induced by a pump pulse at 560 nm with intensity of 110 μJ/cm^2. Starting from the carrier distribution excited by plasmon decay at $t = 0$, electron-electron scattering concentrates the distribution near the Fermi level with the peak optical signal at ~700 fs, followed by a return to the ambient-temperature Fermi distribution and a decay of the optical signal due to electron-phonon scattering.

described next. From those, we calculate the variation of the metal dielectric function $\epsilon(\omega, t)$ and, in turn, the extinction cross section using Mie theory [42,43]. To minimize systematic errors between theory and experiment, we add the *ab initio* prediction for the change in the dielectric function from ambient temperature [33] to the experimental dielectric functions from ellipsometry [44].

We calculate the time evolution of the carrier distributions using the nonlinear Boltzmann equation:

$$\frac{d}{dt}f(\varepsilon,t) = \Gamma_{e\text{-}e}[f](\varepsilon) + \Gamma_{e\text{-ph}}[f, T_l](\varepsilon), \tag{2}$$

where $\Gamma_{e\text{-}e}$ and $\Gamma_{e\text{-ph}}$, respectively, are the contributions due to electron-electron and electron-phonon interactions to the collision integral. For simplicity, we assume that the phonons remain thermal at an effective temperature $T_l(t)$ and calculate the time evolution of the lattice temperature using energy balance, $-C_l(T_l)(dT_l/dt) = (dE/dt)|_{e\text{-ph}}$, where the term on the right corresponds to the rate of energy transfer from the lattice to the electrons due to $\Gamma_{e\text{-ph}}$, and C_l is the *ab initio* lattice heat capacity [33].

The *ab initio* collision integrals are extremely computationally expensive to calculate repeatedly to directly solve Eq. (2). We therefore use simpler models for the collision integrals parametrized using *ab initio* calculations. For electron-electron scattering in plasmonic metals, the calculated electron lifetimes exhibit the inverse quadratic energy dependence $\tau^{-1}(\varepsilon) \approx (D_e/\hbar)(\varepsilon - \varepsilon_F)^2$ characteristic of free-electron models within Fermi liquid theory [17]. We therefore use the free-electron collision integral [20,26,45],

$$\begin{aligned}\Gamma_{e\text{-}e}[f](\varepsilon) = \frac{2D_e}{\hbar}\int d\varepsilon_1 d\varepsilon_2 d\varepsilon_3 \frac{g(\varepsilon_1)g(\varepsilon_2)g(\varepsilon_3)}{g^3(\varepsilon_F)} \\ \times \delta(\varepsilon + \varepsilon_1 - \varepsilon_2 - \varepsilon_3) \\ \times \{f(\varepsilon_2)f(\varepsilon_3)[1 - f(\varepsilon)][1 - f(\varepsilon_1)] \\ - f(\varepsilon)f(\varepsilon_1)[1 - f(\varepsilon_2)][1 - f(\varepsilon_3)]\},\end{aligned} \tag{3}$$

with the constant of proportionality D_e extracted from *ab initio* calculations of electron lifetimes [33]. In doing so, we neglect variation of the electron-electron scattering rate between states with different momenta at the same energy, which is an excellent approximation for gold where this variation is ~10% for energies within 5 eV of the Fermi level [17]. For electron-phonon scattering, assuming that phonon energies are negligible on the electronic energy scale (an excellent approximation for optical frequency excitations in metals), we can simplify the electron-phonon collision integral to

$$\begin{aligned}&\Gamma_{e\text{-ph}}[f, T_l](\varepsilon) \\ &= \frac{1}{g(\varepsilon)}\frac{\partial}{\partial\varepsilon}\left[H(\varepsilon)\left(f(\varepsilon)[1 - f(\varepsilon)] + k_B T_l \frac{\partial f}{\partial\varepsilon}\right)\right],\end{aligned} \tag{4}$$

where $H(\varepsilon)$ is an energy-resolved electron-phonon coupling strength calculated from *ab initio* electron-phonon matrix elements [33]. (See Supplemental Material [39] for details, derivations, and plots, as well as numerical tabulation of $H(\varepsilon)$ for four commonly used plasmonic metals: the noble metals and aluminum).

In our experiments, we use an ultrafast transient absorption system with a tunable pump and white-light probe to measure the extinction of Au colloids in solution as a function of pump-probe delay time and probe wavelength. The laser system consists of a regeneratively amplified Ti: sapphire oscillator (Coherent Libra), which delivers 1-mJ pulse energies centered at 800 nm with a 1-kHz repetition rate. The pulse duration of the amplified pulse is approximately 50 fs. The laser output is split by an optical wedge to produce the pump and probe beams and the pump beam wavelength is tuned using a coherent OperA optical parametric amplifier. The probe beam is focused onto a sapphire plate to generate a white-light continuum probe. The time-resolved differential extinction spectra are collected with a commercial Helios absorption spectrometer (Ultrafast Systems LLC). The temporal behavior is monitored by increasing the path length of the probe pulse and delaying it with respect to the pump pulse with a linear translation stage capable of step sizes as small as 7 fs. Our sample is a solution of 60-nm-diameter Au colloids in water with a concentration of 2.6×10^{10} particles per milliliter (BBI International, EM.GC60, OD1.2) in a quartz cuvette with a 2-mm path length.

The initial excitation by the pump pulse generates an electron distribution that is far from equilibrium, for which temperature is not well defined. Our *ab initio* predictions of the carrier distribution at $t = 0$ in Fig. 2 exhibit high-energy holes in the *d* bands of gold and lower-energy electrons near the Fermi level. These highly nonthermal carriers rapidly decay within 100 fs, resulting in carriers closer to the Fermi level which thermalize via electron-electron scattering in several 100 fs, reaching a peak higher-temperature thermal distribution at ~700 fs in the example shown in Fig. 2. These thermalized carriers then lose energy to the lattice via electron-phonon scattering over several picoseconds.

The conventional two-temperature analysis is only valid in that last phase of signal decay (beyond 1 ps) once the electrons have thermalized. The initial response additionally includes contributions from short-lived highly nonthermal carriers excited initially, which become particularly important at low pump powers when smaller temperature changes limit the thermal contribution. Higher-energy nonthermal carriers exhibit faster rise and decay times than the thermal carriers closer to the Fermi level [26,35], due to higher electron-electron scattering rates. Their response also spans a greater range in probe wavelength compared to thermal electrons, which primarily affect only the resonant *d* band to Fermi level transition [26,33,46], Combining *ab initio* predictions and experimental measurements of 60-nm colloidal

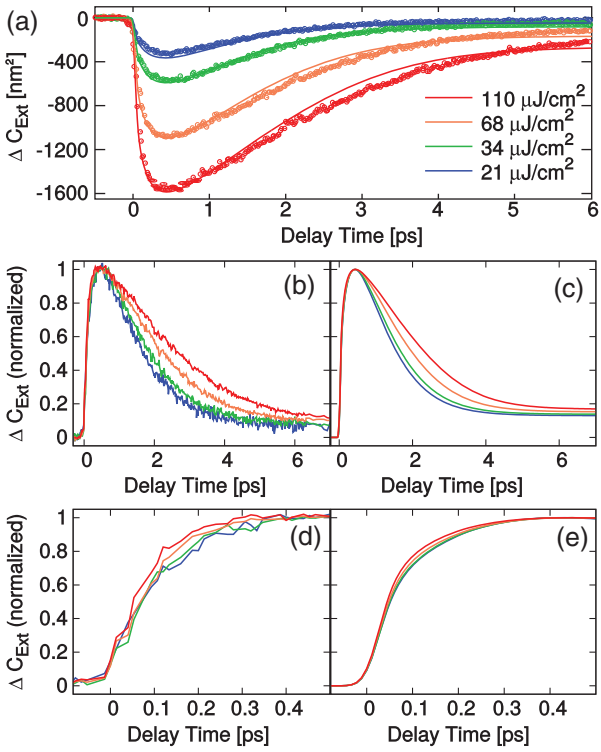

FIG. 3. Comparison of measured and predicted differential cross sections at 530-nm probe wavelength for pump excitation at 560 nm with intensities of 21, 34, 68, and 110 μJ/cm^2 as a function of time. Panel (a) compares absolute measurements (circles) and calculated values (solid lines) of the differential cross section, while the remaining panels are normalized by the peak value: (b) and (c) show measurements and predictions, respectively, over the full time range, while (d) and (e) focus on the initial rise period. Increased pump power generates more initial carriers, which equilibrate faster (shorter rise time) to a higher electron temperature (larger signal amplitude), which subsequently relaxes more slowly due to increased electron heat capacity. The *ab initio* predictions quantitatively match all these features of the measurements.

gold solutions, we quantitatively identify these signatures of thermal and nonthermal electrons, first as a function of pump power and then as a function of probe wavelength.

Figure 3(a) first shows that our *ab initio* predictions of electron dynamics and optical response quantitatively capture the *absolute* extinction cross section as a function of time for various pump pulse energies. Note that the agreement is uniformly within 10%, which is the level of accuracy that can be expected for parameter-free Density functional theory predictions, given that the first-principles band structures are accurate to 0.1–0.2 eV and optical matrix elements are accurate to 10%–20%, with the larger errors for localized *d* electrons [18]. We then examine the cross section time dependence normalized by peak values to more clearly observe the changes in rise and decay time scales.

Decay of the measured signal is because of energy transfer from electrons to the lattice via electron-phonon scattering. At higher pump pulse energies, the electrons thermalize to a higher temperature. For $T_e < 2000$ K, the electron heat capacity increases linearly with temperature, whereas the electron-phonon coupling strength does not appreciably change with electron temperature [20,33]. Therefore, the electron temperature, and, correspondingly, the measured probe signal, decays more slowly at higher pump powers, as shown in Figs. 3(b) and 3(c). Again, we find quantitative agreement between the measurements and *ab initio* predictions with no empirical parameters.

The rise of the measured signal arises from electron-electron scattering which transfers the energy from few excited nonthermal electrons to several thermalizing electrons closer to the Fermi level. Higher power pump pulses generate a greater number of initial nonthermal carriers, requiring fewer electron-electron collisions to raise the temperature of the background of thermal carriers. Additionally, the electron-electron collision rate increases with temperature because of increased phase space for scattering [20]. Both these effects lead to a faster rise time at higher pump powers, as seen in the measurements shown in Fig. 3(d), as well as in the *ab initio* predictions shown in Fig. 3(e), once again in quantitative agreement.

Next, we examine the variation of the ratio of thermal and nonthermal electron contributions with pump power. Figure 4 shows the subpicosecond variation of measured response for two different pump powers, but now with a pump wavelength of 380 nm with a higher-energy photon that excites nonthermal carriers further from the Fermi level. Additionally, the probe wavelength of 560 nm is far from the interband resonance at ~520 nm, so that the thermal electrons contribute less to the measured response. The response has a slow rise and decay time for the higher pump power, as observed previously in cases where thermal electrons dominate. However, for the lower pump power, the thermal contribution is smaller, making the nonthermal contribution relatively more important, resulting in a faster rise and decay time. Once again, the

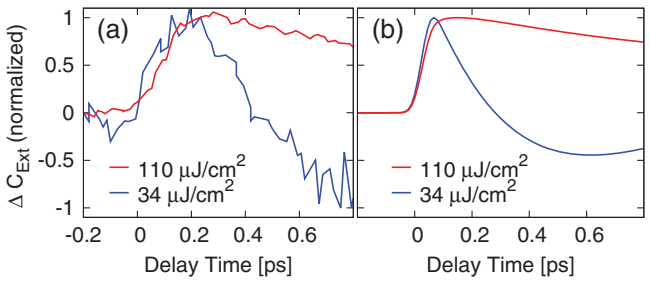

FIG. 4. (a) Measured and (b) calculated differential cross sections normalized by peak value for 380-nm pump pulse with 34- and 110-μJ/cm^2 intensities, monitored at 560-nm probe wavelength. Contributions from the nonthermal electrons dominate at lower pump power, resulting in a fast signal rise and decay. [Correspondingly, smaller signals cause the higher relative noise in the measurements shown in (a).]

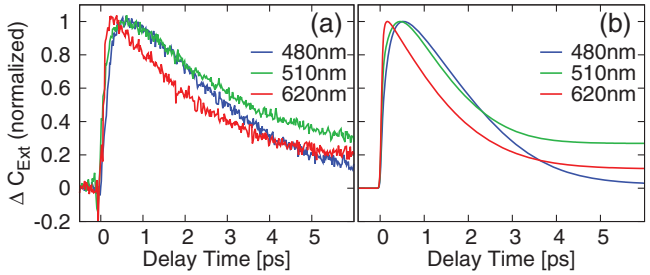

FIG. 5. (a) Measured and (b) calculated differential cross sections for 560-nm pump pulse with 110-μJ/cm^2 intensity, normalized by peak value, for probe wavelengths of 480, 510, and 620 nm. Rise and decay are faster for probe wavelengths far from the interband resonance at 530 nm, where nonthermal effects are relatively more important.

measurements and *ab initio* calculations, which include all these effects implicitly, are in quantitative agreement.

Finally, we examine the variation of the temporal signatures with probe wavelength. Thermalized electrons in noble metals predominantly contribute near the resonant $d \rightarrow s$ transitions, and, therefore, nonthermal signatures become relatively more important at probe wavelengths far from these resonances. Figure 5(a) indeed shows a faster rise and decay due to nonthermal electrons for a probe wavelength of 620 nm, compared to that at 510 nm, which is near the interband resonance (530 nm). Capturing the wavelength dependence of the dielectric function in simple theoretical models [26] is challenging because it involves simultaneous contributions from a continuum of electronic transitions with varying matrix elements. Our *ab initio* calculations [Fig. 5(b)] implicitly account for all these transitions and are therefore able to match both the spectral and temporal features of the measurements, with no empirical parameters.

To conclude, by combining the first-principles calculations of carrier dynamics and optical response, this Letter presents a complete theoretical description of pump-probe measurements, free of any fitting parameters that are typical in previous analyses [35,47–49]. The theory here accounts for detailed energy distributions of excited carriers (Fig. 2) instead of assuming flat distributions [36,37,45], and accounts for electronic-structure effects in the density of states, electron-phonon coupling, and dielectric functions beyond the empirical free-electron or parabolic band models previously employed [20,26,37,45,47–52]. This framework, by leveraging Wannier interpolation of electron-phonon matrix elements, enables quantitative predictions, while avoiding the empiricism that could hide cancellation of errors or obscure physical interpretation of experimental data. For example, we clearly identified the temporal and spectral signatures of short-lived highly nonthermal initial carriers and the longer-lived thermalizing carriers near the Fermi level in plasmonic nanoparticles. By demonstrating the predictive capabilities of our theory for metal nanoparticles, we open up the field for similar studies in other materials [53] where fits are not necessarily possible or even reliable, e.g., semiconductor plasmonics, and where *ab initio* theory of ultrafast dynamics will be indispensable.

This material is based upon work performed by the Joint Center for Artificial Photosynthesis, a DOE Energy Innovation Hub, supported through the Office of Science of the U.S. Department of Energy under Award No. DE-SC0004993. Work at the Molecular Foundry was supported by the Office of Science, Office of Basic Energy Sciences, of the U.S. Department of Energy under Contract No. DE-AC02-05CH11231. The authors acknowledge support from NG NEXT at Northrop Grumman Corporation. Calculations in this work used the National Energy Research Scientific Computing Center, a DOE Office of Science User Facility supported by the Office of Science of the U.S. Department of Energy under Contract No. DE-AC02-05CH11231. P. N. is supported by a National Science Foundation Graduate Research Fellowship and by the Resnick Sustainability Institute. A. M. B. is supported by a National Science Foundation Graduate Research Fellowship, a Link Foundation Energy Fellowship, and the DOE "Light-Material Interactions in Energy Conversion" Energy Frontier Research Center (DE-SC0001293).

*sundar@rpi.edu
†prineha@caltech.edu

[1] M. L. Brongersma, N. J. Halas, and P. Nordlander, Nat. Nanotechnol. **10**, 25 (2015).
[2] H. A. Atwater and A. Polman, Nat. Mater. **9**, 205 (2010).
[3] A. J. Leenheer, P. Narang, N. S. Lewis, and H. A. Atwater, J. Appl. Phys. **115**, 134301 (2014).
[4] T. P. White and K. R. Catchpole, Appl. Phys. Lett. **101**, 073905 (2012).
[5] P. Narang, R. Sundararaman, and H. A. Atwater, Nanophotonics **5**, 96 (2016).
[6] S. Linic, P. Christopher, H. Xin, and A. Marimuthu, Acc. Chem. Res. **46**, 1890 (2013).
[7] S. Mukherjee, F. Libisch, and N. Large, Nano Lett. **13**, 240 (2013).
[8] C. Clavero, Nat. Photonics **8**, 95 (2014).
[9] S. Linic, U. Aslam, C. Boerigter, and M. Morabito, Nat. Mater. **14**, 567 (2015).
[10] M. Moskovits, Nat. Nanotechol. **10**, 6 (2015).
[11] H. Harutyunyan, A. B. F. Martinson, D. Rosenmann, L. K. Khorashad, L. V. Besteiro, A. O. Govorov, and G. P. Wiederrecht, Nat. Nanotechnol. **10**, 770 (2015).
[12] M. Zavelani-Rossi, D. Polli, S. Kochtcheev, A.-L. Baudrion, J. Béal, V. Kumar, E. Molotokaite, M. Marangoni, S. Longhi, G. Cerullo, P.-M. Adam, and G. D. Valle, ACS Photonics **2**, 521 (2015).
[13] A. O. Govorov, H. Zhang, and Y. K. Gun'ko, J. Phys. Chem. C **117**, 16616 (2013).

[14] V. E. Babicheva, S. V. Zhukovsky, R. S. Ikhsanov, I. E. Protsenko, I. V. Smetanin, and A. Uskov, ACS Photonics **2**, 1039 (2015).
[15] A. O. Govorov, H. Zhang, H. V. Demir, and Y. K. Gun'ko, Nano Today **9**, 85 (2014).
[16] M. Conforti and G. D. Valle, Phys. Rev. B **85**, 245423 (2012).
[17] A. Brown, R. Sundararaman, P. Narang, W. A. Goddard III, and H. A. Atwater, ACS Nano **10**, 957 (2016).
[18] R. Sundararaman, P. Narang, A. S. Jermyn, W. A. Goddard III, and H. A. Atwater, Nat. Commun. **5**, 5788 (2014).
[19] S. I. Anisimov, B. L. Kapeliovich, and T. L. Perelman, Zh. Eksp. Teor. Fiz. **66**, 375 (1974).
[20] N. D. Fatti, C. Voisin, M. Achermann, S. Tzortzakis, D. Christofilos, and F. Vallée, Phys. Rev. B **61**, 16956 (2000).
[21] H. Elsayed-Ali, T. Norris, M. Pessot, and G. Mourou, Phys. Rev. Lett. **58**, 1212 (1987).
[22] H. E. Elsayed-Ali, T. Juhasz, G. O. Smith, and W. E. Bron, Phys. Rev. B **43**, 4488 (1991).
[23] A. Giri, E. M. Kirkpatrick, P. Moongkhamklang, S. A. Majetich, and V. G. Harris, Appl. Phys. Lett **80**, 2341 (2016).
[24] G. V. Hartland, Chem. Rev. **111**, 3858 (2011).
[25] M. I. Kaganov, I. M. Lifshitz, and L. V. Tanatarov, Sov. Phys. JETP **4**, 173 (1957).
[26] C.-K. Sun, F. Vallée, L. H. Acioli, E. P. Ippen, and J. G. Fujimoto, Phys. Rev. B **50**, 15337 (1994).
[27] R. H. Groeneveld, R. Sprik, and A. Lagendijk, Phys. Rev. B **51**, 11433 (1995).
[28] E. Knoesel, A. Hotzel, and M. Wolf, Phys. Rev. B **57**, 12812 (1998).
[29] M. Aeschlimann, M. Bauer, S. Pawlik, W. Weber, R. Burgermeister, D. Oberli, and H. Siegmann, Phys. Rev. Lett. **79**, 5158 (1997).
[30] J. Hohlfeld, E. Matthias, R. Knorren, and K. Bennemann, Phys. Rev. Lett. **78**, 4861 (1997).
[31] S. Brorson, J. Fujimoto, and E. Ippen, Phys. Rev. Lett. **59**, 1962 (1987).
[32] N. Rotenberg, A. D. Bristow, M. Pfeiffer, M. Betz, and H. M. van Driel, Phys. Rev. B **75**, 155426 (2007).
[33] A. M. Brown, R. Sundararaman, P. Narang, W. A. Goddard III, and H. A. Atwater, Phys. Rev. B **94**, 075120 (2016).
[34] N. Rotenberg, J. N. Caspers, and H. M. van Driel, Phys. Rev. B **80**, 245420 (2009).
[35] X. Shen, Y. P. Timalsina, T.-M. Lu, and M. Yamaguchi, Phys. Rev. B **91**, 045129 (2015).
[36] G. D. Valle, M. Conforti, S. Longhi, G. Cerullo, and D. Brida, Phys. Rev. B **86**, 155139 (2012).
[37] C. Voisin, N. D. Fatti, D. Christofilos, and F. Vallée, J. Phys. Chem. B **105**, 2264 (2001).
[38] A. Giri and P. E. Hopkins, J. Appl. Phys. **118**, 215101 (2015).
[39] See Supplemental Material at http://link.aps.org/supplemental/10.1103/PhysRevLett.118.087401 for the derivations relevant to the manuscript.
[40] R. Sundararaman, D. Gunceler, K. Letchworth-Weaver, and T. A. Arias, http://jdftx.sourceforge.net.
[41] I. Souza, N. Marzari, and D. Vanderbilt, Phys. Rev. B **65**, 035109 (2001).
[42] G. Mie, Ann. Phys. (Berlin) **330**, 377 (1908).
[43] C. Matzler, Institut fur Angewandte Physik Tecnical Report No. 2002-08, 2002.
[44] E. D. Palik, *Handbook of Optical Constants of Solids* (Academic, New York, 1985).
[45] B. Mueller and B. Rethfeld, Phys. Rev. B **87**, 035139 (2013).
[46] J. Hohlfeld, S.-S. Wellershoff, J. Güdde, U. Conrad, V. Jähnke, and E. Matthias, Chem. Phys. **251**, 237 (2000).
[47] A. Giri, J. T. Gaskins, B. M. Foley, R. Cheaito, and P. E. Hopkins, J. Appl. Phys. **117**, 044305 (2015).
[48] P. M. Norris, A. P. Caffrey, R. J. Stevens, J. M. Klopf, J. T. McLeskey, and A. N. Smith, Rev. Sci. Instrum. **74**, 400 (2003).
[49] R. Rosei, F. Antonangeli, and U. Grassano, Surf. Sci. **37**, 689 (1973).
[50] Z. Lin, L. V. Zhigilei, and V. Celli, Phys. Rev. B **77**, 075133 (2008).
[51] X. Y. Wang, D. M. Riffe, Y.-S. Lee, and M. C. Downer, Phys. Rev. B **50**, 8016 (1994).
[52] B. Rethfeld, A. Kaiser, M. Vicanek, and G. Simon, Phys. Rev. B **65**, 214303 (2002).
[53] A. Alkauskas, M. D. McCluskey, and C. G. Van de Walle, J. Appl. Phys. **119**, 181101 (2016).